Advanced Materials Technologies

ADVANCED MATERIALS TECHNOLOGIES
www.advmattechnol.com

Research Article OPEN ACCESS

Design and Fabrication of High Dielectric GRIN Lens for a Directive Antenna Using a Hybrid Filled Voxel Additive Manufacturing Technique

Qianfang Zheng[1] | Anna Radkovskaya[2] | Kailun Xu[2] | Ekaterina Shamonina[2] | Patrick S. Grant[1]

[1]Department of Materials, University of Oxford, Parks Road, Oxford, UK | [2]Department of Engineering Science, University of Oxford, Parks Road, Oxford, UK

Correspondence: Qianfang Zheng (qianfang.zheng@materials.ox.ac.uk) | Patrick S. Grant (patrick.grant@materials.ox.ac.uk)

Received: 17 August 2025 | **Revised:** 31 October 2025 | **Accepted:** 16 November 2025

Keywords: additive manufacturing | antennas | dielectric composites | gradient index lens | metamaterials

ABSTRACT

Additive manufacturing (AM) has been used to produce materials and structural components with graded or anisotropic mechanical properties, primarily through variations in local porosity. However, beyond structural applications, there are significant technological opportunities for additively manufactured devices with spatial gradations of functional properties, such as magnetic and dielectric properties, to provide novel device functionality. This paper describes a hybrid filled voxel AM technique for producing devices with 3D, spatially graded relative permittivity. The approach is illustrated through simulation-informed design, fabrication, and microwave characterization of a filled voxel dielectric gradient refractive-index (GRIN) lens that combines a 3D-printed polymer lattice with a manual additive assembly of pre-densified dielectric voxels of tailored permittivity. The hybrid-AM GRIN lens enabled a significant reduction in the length of a transmitting microwave antenna horn by 50%, while also enhancing its directivity from 6.75 to 7.74 dB at 15 GHz. We demonstrate the potential of filled voxel hybrid-AM graded devices to improve microwave device performance and to facilitate miniaturization.

1 | Introduction

Microwave lenses are key components in microwave engineering and electromagnetics, where they are used to convert a plane wave into a spherical wave, focusing microwave radiation to a point, or to transform microwaves from a feed into a planar wavefront, thus collimating the beam. These manipulations enable the enhancement of microwave antenna performance through beamforming, increased gain, and improved directivity [1]. Conventional refractive lenses, typically featuring convex, or spherical shapes, are often considered unsuitable for microwave antenna systems due to design limitations such as their large size and weight [2]. In contrast, flat lenses that are lightweight and low-profile have attracted growing interest [3], utilizing ideas from transformation optics [4,5], geometrical optics [6,7], field transformations [8,9], and topology optimization [10].

For controlling electromagnetic wave propagation, flat lenses are typically designed with a spatially varying refractive index. Achieving a gradient index (GRIN) lens presents significant challenges to conventional manufacturing techniques, but are being progressively addressed. For example, metallic resonant elements were employed as subwavelength units to construct metamaterial structures that were fabricated into GRIN lenses [11–13]. However, metamaterial-based lenses typically suffer from a narrow bandwidth, substantial energy loss,

Patrick S. Grant and Qianfang Zheng are co-corresponding authors.

fabrication complexities, and high cost that restrict their broader use [14].

Additive manufacturing (AM) has recently emerged as a promising method for producing graded and anisotropic structures. Various AM technologies, including direct ink writing (DIW) [15], grayscale digital light processing voxel printing (gDLP-VPP) [16], and two-photon polymerization (2PP) [17], have been employed to fabricate GRIN lenses in the optical domain, demonstrating the capability of AM to achieve finely controlled, continuous refractive-index gradients across scales, with high spatial precision and design flexibility. However, translating these AM approaches to the microwave regime remains challenging due to the larger device dimensions resulting from longer wavelengths, and the need for material systems that meet electromagnetic property requirements. A growing body of studies has begun to explore these challenges. For example, creating air voids and manipulating local porosity fraction within a printed polymer has enabled graded and anisotropic effective refractive indices [18–20]. This arises because refractive index n is related to local permittivity ε and permeability μ by $n = \sqrt{\varepsilon\mu}$, and n can be manipulated by local changes in the proportion of air ($\varepsilon = 1$) and an AM polymer ($\varepsilon = 2 - 2.7$ [21]). Although this approach is relatively simple and leverages the advantages of AM, the range of the attainable refractive indices is inherently limited to values bounded by the dielectric properties of the polymer and air. This constrains the refractive index "contrast" achievable across the lens and, subsequently, the device miniaturization potential.

One strategy to broaden the achievable refractive index range in these devices is to fill the voids in the 3D printed polymer lattice with a high-permittivity liquid medium [22, 23]. This approach has achieved a local permittivity of up to 42 [24], and a GRIN Eaton lens was fabricated by combining a 3D-printed woodpile structure with infilling using a compound liquid medium composed of benzene and acetonitrile [25]. By adjusting the volume filling fraction of the constituent materials and the composition of the benzene/acetonitrile mixture, a permittivity range from 1 (air) to 40 was realized. However, devices utilizing a liquid medium face limitations due to limited temperature range, leakage and high loss [26].

Alternatively, composite polymer filaments with high dielectric permittivity, such as an acrylonitrile butadiene styrene (ABS)/ferroelectric barium titanate ($BaTiO_3$) composite, can be printed to provide a permittivity of up to 11 [27–29]. By varying the volume-weighted local proportion of high-permittivity ABS/$BaTiO_3$ and low-permittivity ABS only, in conjunction with different azimuthal rotations, a flat spiral phase plate (SPP) with a gradient effective permittivity ranging from 2.65 to 11 was fabricated [30]. However, filaments with a high fraction (up to 70 wt.%) of high dielectric ceramic powders such as $BaTiO_3$ are susceptible to breakage and nozzle clogging during printing. Furthermore, the detailed structures required and multi-material AM can extend print times to many hours or even days.

Beyond filament-based extrusion, other extrusion-based AM techniques such as DIW and ambient reactive extrusion (ARE) have also shown potential for fabricating compositionally graded functional composites [31–33]. For instance, by either printing porous structures using a single high–filler-loaded dielectric ink to vary the local air fraction [34], or actively mixing high- and low-permittivity inks during extrusion to continuously tune the filler ratio [35], these approaches have allowed a relative permittivity gradient to be engineered. However, both methods demand rheological tuning for successful fabrication and additional post-processing, including sintering or extended curing, which hinders their scalability for larger microwave components.

In this paper, we introduce a hybrid-AM "filled voxel" approach for fabricating GRIN lenses designed for operation within the 12–18 GHz frequency range. We use the lens to enable a reduction in the physical dimensions of a conventional horn antenna, while investigating the associated effects on antenna gain and directivity. Faced with the challenge of printing the lens with a continuous variation in relative permittivity, we discretize the radially graded dielectric constant into elementary 3D units termed voxels. To realize this discretized design in practice, seven pre-made ABS/$BaTiO_3$ polymer composites with different $BaTiO_3$ fractions and thus distinct permittivities are prepared, forming a dielectric "color" palette. Each voxel within a 3D-printed lens lattice is then additively assembled by hand from a calculated mixture of the dielectric colors. This dual-additive route combines the precision of 3D printing with the voxel-wise control of dielectric composition. A GRIN lens is chosen to facilitate a reduction in an idealized microwave horn antenna length by up to threefold, while aiming to maintain key performance metrics in gain and directivity. To obtain the required spatial variation of permittivity in the lens, finite-element-based simulations were used. The hybrid-AM GRIN lens performance in experiment aligns closely with simulations, and the compact microwave horn coupled with the GRIN lens enhances directivity compared with an optimized reference horn operating over the same frequency range.

2 | Design of the GRIN Lens and Horn Antenna

A horn antenna, a fundamental and extensively utilized device in microwave engineering, is frequently employed either as a feed and/or as a receiving element within a communication system. Horns offer a straightforward design and construction process, good broadband performance, exceptional directionality, and significant gain. In this study, a H-plane sectoral horn antenna was selected because of its simplicity and good overall performance [21].

Optimal directivity for a H-plane horn antenna is obtained when its geometric dimensions satisfy the condition $A = \sqrt{3\lambda R}$ where A is the H-plane aperture width of the horn, R is the distance from the phase center to the edge of the horn (designed to be equal to the horn length in this study), and λ is the operating wavelength [36]. Here, a reference horn was selected to operate at a frequency of 15 GHz, with R_{ref} set to 6λ (120 mm) and A_{ref} to $3\sqrt{2}\lambda$ (84 mm). Because microwave horns can be quite large, related to the wavelength, there is interest in miniaturization while maintaining performance. Therefore, we also chose a compact horn, shortened to a non-optimized length of 2λ (40 mm), and which ordinarily could be expected to yield a significant loss of performance. Based on our prior work using a different fabrication approach [21], our hypothesis is that by adding a filled voxel GRIN lens to the shortened horn,

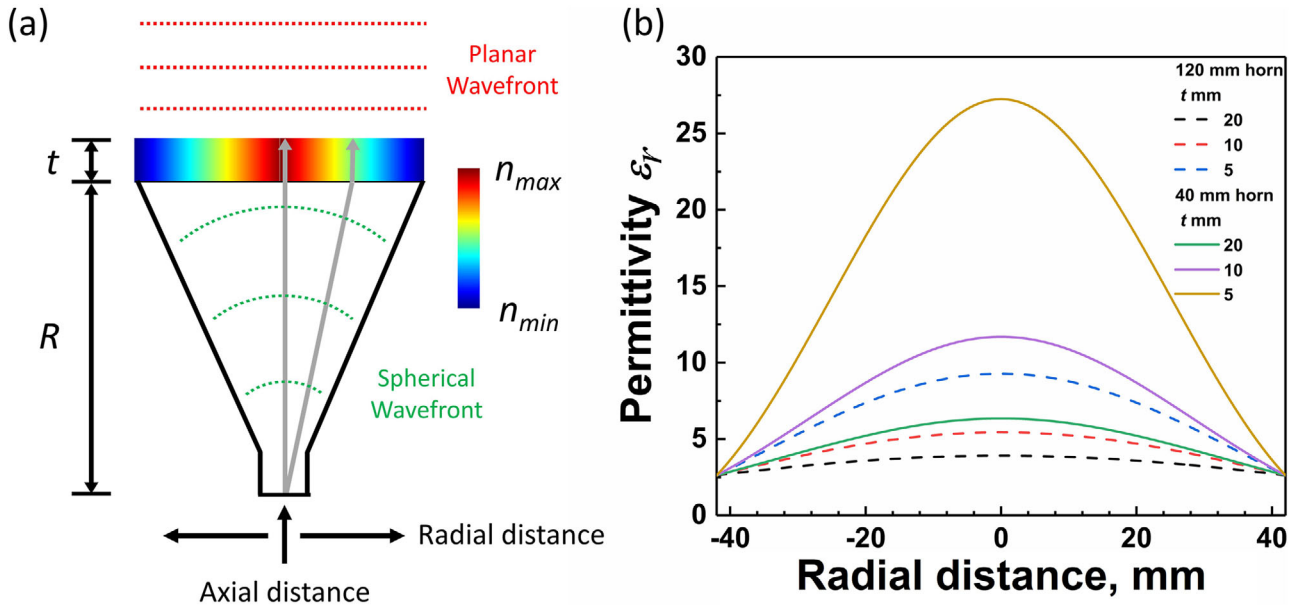

FIGURE 1 | (a) Schematic diagram of the GRIN lens, (b) distribution of relative dielectric permittivity for different thicknesses of the GRIN lens, comparing the reference horn (120 mm, dashed lines) with the shortened horn (40 mm, solid lines).

performance close to optimum can be recovered. Fundamentally, to recover the directivity of the compact horn, the GRIN lens must efficiently transform the otherwise spherical wavefront emitted by the non-optimum horn back into a planar wavefront.

This transformation necessitates that electromagnetic waves exiting the lens at any radial location exhibit uniform phase velocity delay, as depicted in Figure 1a, implying the necessity for a lens with a radially varying refractive index [37]. The refractive index distribution profile for a GRIN lens, as a function of radial distance from the lens center, is described by [21]:

$$n(r) = n(0) - \frac{\sqrt{r^2 + R^2} - R}{t} \tag{1}$$

where $n(r)$ and $n(0)$ are the refractive index at a radial distance r and at the lens center, respectively, and t is the lens thickness.

Equation (1) demonstrates that enhancing the "contrast" – or range – in refractive index across the lens ($\Delta n = n_{max} - n_{min}$) facilitates a reduction in both the horn length R and lens thickness t (and therefore weight). Figure 1b illustrates the radial distribution of relative dielectric permittivity $\varepsilon_r(r)$, for a non-magnetic ($n = \sqrt{\varepsilon\mu}, \mu = 1$) GRIN lens with an aperture $A = 84$ mm, for a range of lengths R and thicknesses t.

To evaluate the microwave performance of various horns and GRIN lenses, simulations were conducted using COMSOL Multiphysics RF Module, a commercial finite-element analysis software. Simulations were used to predict the far-field or "free space" radiation patterns emitted by different horn designs. For example, Figure 2 shows the simulated electric field distribution at 15 GHz for three configurations: the reference horn with $R_{ref} = 6\lambda$ (Figure 2a), a shortened horn with $R_{short} = 2\lambda$ (Figure 2b), and a shortened horn coupled with a 20 mm thick GRIN lens featuring an ideal, continuous graded permittivity profile according to Equation (1) (Figure 2c). To mitigate reflections and to minimize overall loss due to the presence of the lens over the open aperture of the shortened horn, the design and simulation of the GRIN lens also incorporated a 3 mm thick input and output impedance matching layer with $\varepsilon = 2.62$, based on simulations. The three antennas had the same aperture size ($A = 84$ mm), but there was significant wave broadening and reduced directivity when the horn length was reduced by two-thirds. However, coupling with the GRIN lens resulted in a notable refocusing of the outgoing beam. These comparisons are analyzed in more detail in subsequent sections.

3 | GRIN Lens Simulations Using a Discretized Model

To fabricate the GRIN lens in practice, it is necessary to discretize the ideal, continuous permittivity distribution along the radial direction into discrete elements or voxels. This involved a step-wise approximation of the continuous permittivity profile using a specific number of discrete composite elements N_{rad}. In this case and as illustrated in Figure 3, each voxel was chosen of uniform dimensions. The voxel width r_{rad} is calculated from:

$$r_{\text{rad}} = \frac{A - (N_{\text{rad}} + 1)r_l}{N_{\text{rad}}} \tag{2}$$

where r_l is the thickness of the voxel wall in the lattice structure.

As N_{rad} increased (and r_{rad} correspondingly decreased), the arrangement in Figure 3 tended toward the ideal, continuous variation in ε, but became more challenging to manufacture. Therefore, to determine the minimum radial discretization number N_{rad} that provided sufficient beam refocusing while maintaining manufacturability, simulations were conducted of the far-field radiation pattern and directivity of a shortened horn

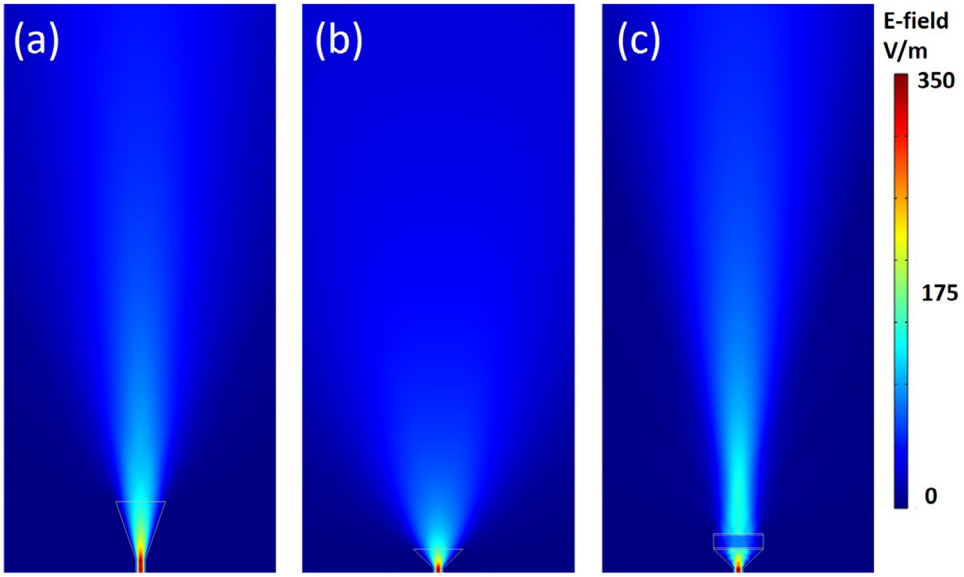

FIGURE 2 | Simulated electric field distribution at 15 GHz for three configurations: (a) a reference horn with $R_{ref} = 6\lambda$, (b) a shortened horn with $R_{short} = 2\lambda$, and (c) a shortened horn coupled with the GRIN lens featuring an ideal continuous graded permittivity profile.

integrated with the GRIN lens for varying N_{rad}. Figure 4a shows the resulting radiation pattern changes. For $N_{rad} = 5$, there were notable and undesirable side lobes in the radiation pattern. As N_{rad} increased, side lobe intensity progressively diminished and the "forward" directivity, at the radial angle of 0°, intensified. Concurrently, the gain of the shortened horn coupled with the GRIN lens also exhibited a slight improvement, increasing from 19.2 to 19.7 dB.

Figure 4b summarizes the simulated directivity performance of the different arrangements, where directivity D is defined as the ratio of the maximum radiated intensity U_{max} to the average power radiated by the horn across all directions, formulated as [36]:

$$D = \frac{U_{\max}}{P/4\pi} = \frac{4\pi U(\theta,\varphi)|_{\max}}{\int_0^{2\pi}\int_0^{\pi} U(\theta,\varphi)\sin\theta d\theta d\varphi} \tag{3}$$

where θ and φ represent the spherical coordinate angles, and P is the total power radiated from the horn. Since the simulations in this work were restricted to the H-plane ($\varphi = \pi/2$), the computed quantity represents the partial directivity within this principal plane. Mirroring the trends observed in the radiation pattern, partial directivity improved with an increase in N_{rad} within the range 5–15, but with only marginal benefits for $N_{rad} \geq 11$. Therefore, the optimal degree of discretization was set as $N_{rad} = 11$.

To construct the discretized GRIN lens with $N_{rad} = 11$ implied six bespoke materials with a specific permittivity of (center to edge) 6.3, 6.2, 5.7, 4.9, 4.0, and 3.1, to fill the appropriate empty voxel in the AM lens voxel framework. However, rather than fabricate these six composite materials directly, it was decided instead to discretize each voxel further into sub-voxels, and to fill each sub-voxel with standard units of composite material of known permittivity, drawn from a dielectric "palette" of materials with permittivities of 3, 4, 5, 6, and 7. These materials were fabricated in bulk as sheets, as described in the Experimental Section. This further discretization of the voxels themselves along the axial direction is depicted in Figure 5a. By stacking different combinations of the standard materials within a voxel, any arbitrary permittivity of the voxel can be achieved to within ± 0.125. The advantage of this approach is that it allows for a more flexible adjustment of lens permittivity profile to suit different applications, from a standard palette of materials.

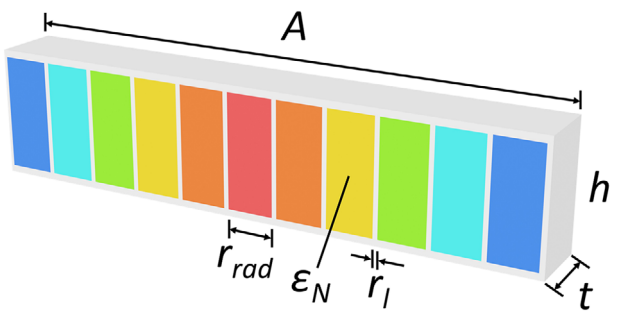

FIGURE 3 | CAD model of the radially symmetric GRIN lens with a discrete radial distribution of permittivity into voxels of uniform size.

In the GRIN lens, microwave propagation can be assumed to occur predominantly in the axial direction. Consequently, the phase velocity delay within a voxel of the lens is determined by the cumulative effect of the stack of sub-voxel composite elements on a ray of incident microwave radiation, with each sub-voxel stack contributing to the overall delay according to the local refraction index n and thickness T according to:

$$\frac{n_{eff}T}{\lambda} = \frac{n_1T_1}{\lambda} + \frac{n_2T_2}{\lambda} + \cdots + \frac{n_NT_N}{\lambda} \tag{4}$$

where n_{eff} is the overall effective refractive index of the voxel, N is the total number of sub-voxel composite elements along the

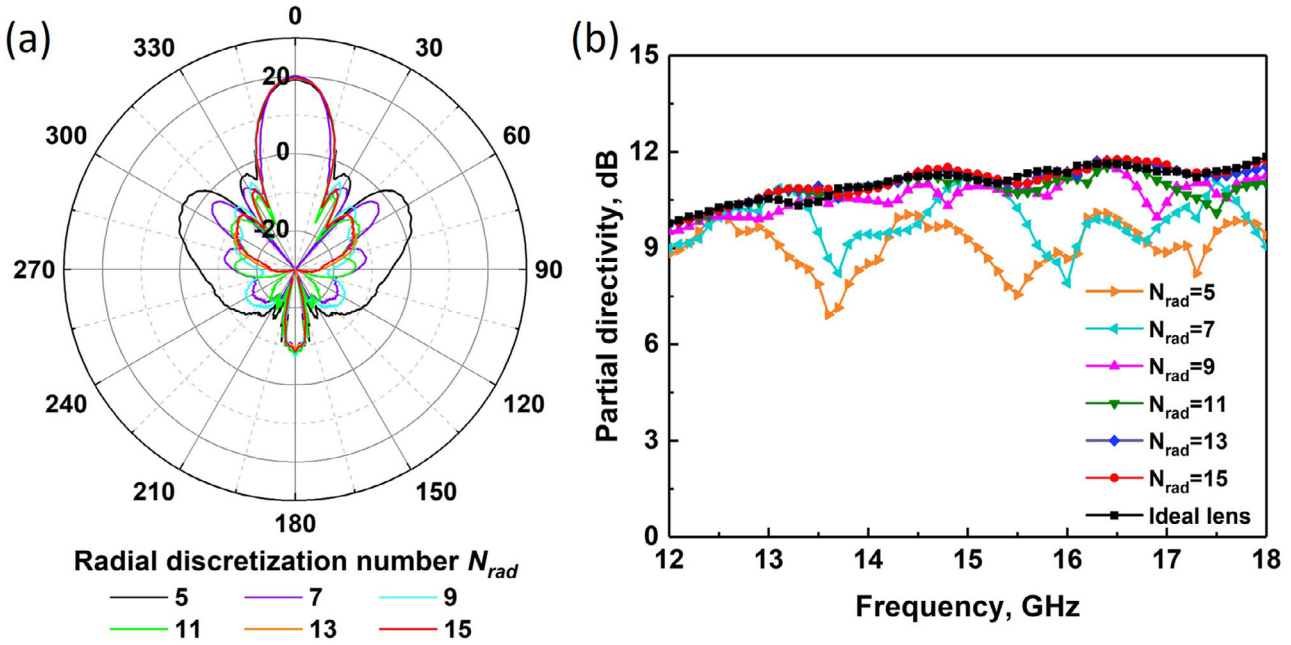

FIGURE 4 | Simulated (a) far-field radiation patterns and (b) directivity of the shortened horn coupled with a filled voxel GRIN lens for different radial discretization number N_{rad}.

axial direction. When the elements are of uniform thickness, the formula simplifies to $n_{eff} = (n_1 + n_2 + \cdots + n_N)/N$. By selecting the right combination of standard elements of permittivities 3, 4, 5, etc., the voxel overall permittivity can be tailored.

Similarly to the radial discretization optimization, to determine the optimal axial discretization number N_{ax}, simulations of the partial directivity of the shortened horn coupled with the GRIN lens for different N_{ax} using sub-voxel elements with permittivities of 3, 4, 5, 6, and 7 were performed. Figure 5b shows the calculated partial directivity in the frequency range 12–18 GHz retrieved from the simulations. Although the directivity showed a slight upward trend as N_{ax} increased from 4 to 20, the improvement was marginal. Specifically, the average partial directivity over the frequency range was 10.24, 10.30, 10.35, and 10.33 dB for N_{ax} = 4, 5, 10, and 20, respectively. Based on this limited variation and considering fabrication efficiency, $N_{ax} = 10$ was selected as the optimal value for the GRIN lens design. Since the discretization optimization was conducted mainly through simulations, the reliability of this simulation-based approach was further verified by comparing the simulated and measured far-field results of the final design, as discussed in Section 4.

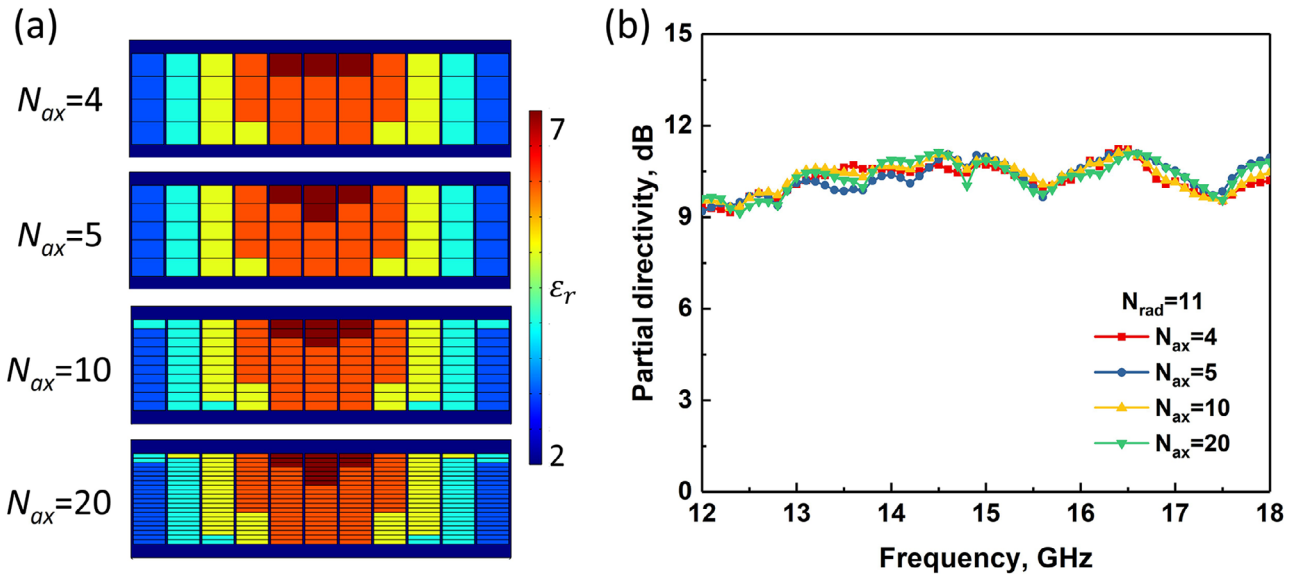

FIGURE 5 | (a) Schematic diagram of the filled voxel GRIN lens discretized for different axial discretization numbers, and (b) the simulated directivity of the shortened horn coupled with a filled voxel GRIN lens for different axial discretization number N_{ax}.

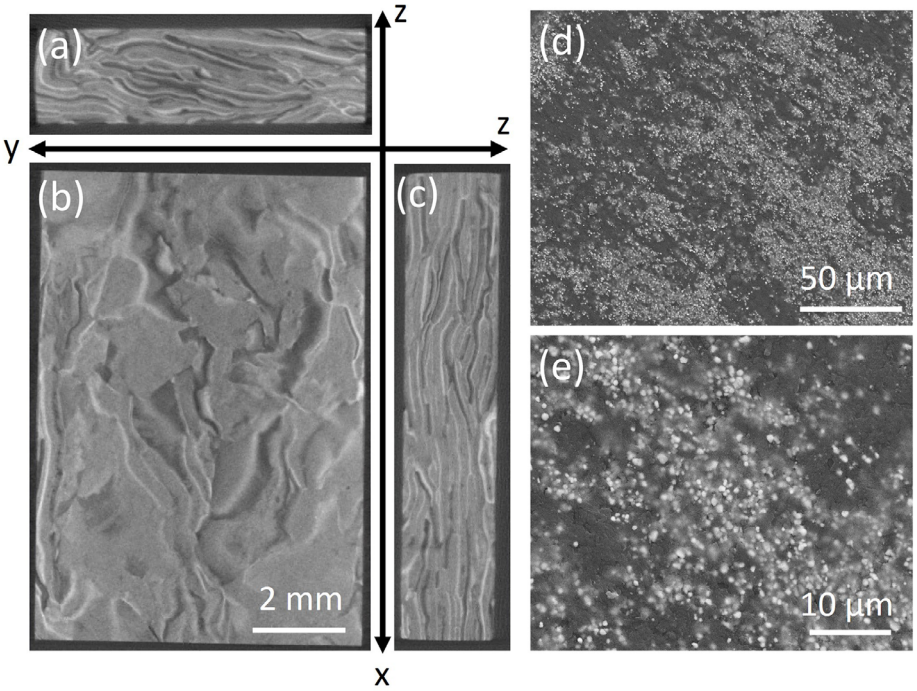

FIGURE 6 | X-ray tomography images in the (a) y-z plane, (b) x-y and (c) x-z plane of the interior of a 20.2 vol.% ABS/$BaTiO_3$ sub-voxel element ($9.8 \times 6.8 \times 2$ mm). (d) Low and (e) high magnification scanning electron micrographs of the cross-section of a 20.2 vol% ABS/$BaTiO_3$ sub-voxel element.

In addition to the discretization parameters, the influence of the wall thickness that forms the lattice containing the empty voxels on the lens performance was also investigated. As shown in Figure S1, the peak gain shows a slight increase from approximately 19.2 to 19.4 dB when the lattice wall thickness (t_{wall}) decreased from 1.0 to 0 mm. The average side-lobe level showed a modest reduction of about 2.8 dB as t_{wall} decreased from 1.0 to 0.5 mm, beyond which the change became marginal. This weak dependence can be mainly attributed to the subwavelength dimension of the lattice walls relative to the operating wavelength at 15 GHz (≈ 20 mm). At such a subwavelength scale, variations in wall thickness only slightly alter the voxel-to-wall volume ratio, leading to a small reduction in the voxel-averaged effective permittivity and, consequently, a minor influence on the overall focusing efficiency. Based on these results, a wall thickness of 0.5 mm was adopted for fabrication, corresponding to the smallest dimension that could be reliably achieved.

4 | GRIN Lens Performance

Figure 6a–c shows three images of internal 2D slices or planes of a composite element, in this case containing 20.2 vol.% $BaTiO_3$, imaged using X-ray computed tomography (XCT). The $BaTiO_3$ particles had strong X-ray absorbance compared with the ABS, and provided the gray level contrast in the image. The brighter regions indicate areas with a higher proportion of $BaTiO_3$. In the x-y plane, $BaTiO_3$ distribution appears relatively random. In contrast, the x-z and y-z planes exhibit a banded structure characterized by elongated, $BaTiO_3$-rich regions aligned parallel to the z-axis, suggesting a layered internal structure within the composite. This non-uniform $BaTiO_3$ distribution resulted from the z-axis pressure during the field-assisted sintering technology (FAST) process, which induced the alignment of the milled composite fragments during polymer flow and consolidation. Overall, there were no large scale voids. Figure 6d,e shows x-y plane cross-sectional scanning electron microscopy (SEM) images of the same 20.2 vol.% $BaTiO_3$ composite element. The particle size of $BaTiO_3$ ranged from 0.3 to 2 µm. At the microscale, there was significant local agglomeration of $BaTiO_3$ particles. However, given the working frequency of 15 GHz, corresponding to a wavelength of 20 mm, the sub-millimeter-scale non-uniformity was assumed to have minimal impact on the overall effective relative permittivity at the frequency of interest.

Representative XCT slices of the composites with low (1.5 vol.%), medium (9.1 vol.%), and high (20.2 vol.%) $BaTiO_3$ fractions are shown in Figure S2. All samples exhibited similar particle banding previously described for Figure 6, irrespective of $BaTiO_3$ fraction.

The permittivities of the materials with $BaTiO_3$ fractions of 1.5, 5.3, 9.1, 12.9, 16.6, 20.2, and 30 vol.% were 2.7, 3.1, 3.8, 4.5, 5.2, 5.8, and 9.6, respectively, with a loss tangent of 6.04×10^{-3}, 1.27×10^{-2}, 1.78×10^{-2}, 2.24×10^{-2}, 2.40×10^{-2}, 2.62×10^{-2}, and 4.83×10^{-2}, respectively. The relationship between $BaTiO_3$ volume fraction and the measured permittivity of the sub-voxel composites is presented in Figure S3. By manually filling the 3D-printed lattice with these sub-voxels in different proportions according to the design (Figure S4), the completed filled voxel GRIN lens was fabricated, whose overall appearance is described later.

Figure 7a–c presents the experimental far-field radiation pattern in the azimuthal plane for the three antenna configurations: the reference horn with $R_{ref} = 6\lambda$, the shortened horn with $R_{short} = 2\lambda$, and the shortened horn coupled with the filled voxel GRIN lens. At 15 GHz, both the reference horn and

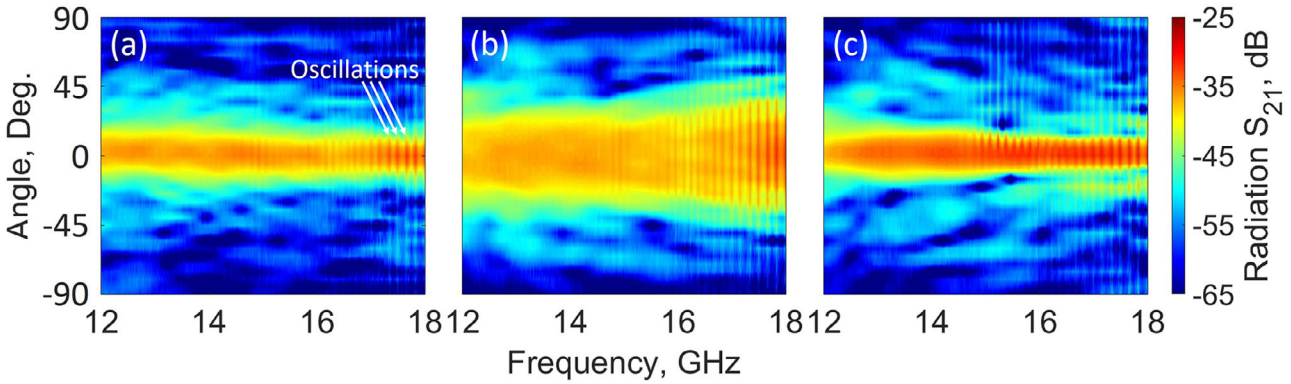

FIGURE 7 | Experimental radiation patterns for (a) the reference horn, (b) the shortened horn, and (c) the shortened horn coupled with the GRIN lens.

the shortened horn with the GRIN lens exhibited significantly more directionality than the 2λ horn without the lens. In the "forward" 0° direction, the transmission coefficient (−32.9 dB) of the shortened horn coupled with the filled voxel GRIN lens exceeded that of the reference horn (−35.4 dB). This highlighted the effectiveness of the filled voxel GRIN lens in enhancing antenna performance, despite the non-optimal, reduced physical dimensions of the horn antenna. The half-power beam width (HPBW) of the reference horn ranged from 11° to 22° across 12–18 GHz, whereas shortening the horn to 2λ increased the HPBW to 31°–57°, indicating a substantial loss of beam confinement. Integration of the GRIN lens into the shortened horn reduced HPBW to 11°–18°, comparable with or narrower than that of the reference horn, depending on frequency. The beamwidth variation across frequency was also smaller, which shows that the lens restores the beamwidth degraded by horn shortening and stabilizes the beam shape over a broad operating band, consistent with the observed directivity enhancement. The oscillations in the experimental radiation pattern, appearing as fringes in the images, were attributed to the non-ideal nature of the receiver horn that led to a super-imposed standing wave between the transmitter and receiver. Additionally, there was a minor deviation of ≈ 3% in the common plane shared by the transmitting and receiving horns that was only detected during post-experiment data processing, but had little effect on the clear trend in the data.

Figure 8a shows the measured partial directivity derived from the radiation patterns for all three antenna systems. This comparison demonstrated the significant reduction in directivity when the horn was shortened to a third of its original length. In contrast, adding the filled voxel GRIN lens to the shortened horn not only compensated for the reduction in performance but significantly enhanced directivity, surpassing that of the reference horn in the 12–17.3 GHz frequency range. Specifically, at 15 GHz, the directivity of the shortened horn coupled with the GRIN lens was 7.74 dB compared with 6.75 dB for the reference horn. These trends closely match the simulation results shown in Figure S5, which also predicted enhanced directivity of the shortened horn when coupled with the filled voxel GRIN lens. The simulated directivities were slightly higher than measured, which may be attributed to minor deviations in geometrical accuracy during printing and the presence of small air gaps between stacked sub-voxels in the assembled lens. Overall, the agreement indicates that the simulation-based discretization model described in Section 3 provides a reliable basis for guiding the lens design. Furthermore, Figure 8b shows the return loss behavior for the same three configurations. All losses were below −10 dB over the 12–18 GHz range, indicating that the horn antenna coupled with the GRIN lens had reasonable impedance matching.

The enhancement of directivity and simultaneous miniaturization of the horn antenna using the filled voxel GRIN lens illustrates the potential of AM to widen traditional design limitations, potentially allowing for more sophisticated and functional microwave devices. A key next step in our approach will be the automation of placing sub-voxel elements into each voxel using a pick-and-place system that, in principle, is readily integrated into our ToolChanger or other modular AM platform. In parallel, extrusion-based AM techniques such as DIW or ARE could also be incorporated as complementary filling routes on the same platform, enabling automated deposition of high-permittivity pastes directly into the printed voxel lattice. This would enable fully "hands-free" GRIN lens manufacturing to improve consistency and scalability, and to significantly reduce production time. Beyond research prototyping, the filled voxel approach is inherently compatible with current additive manufacturing platforms and automated assembly workflows. The modular nature of voxel filling allows integration into multi-material FDM systems or pick-and-place robotic units already widely deployed in electronics manufacturing. This compatibility may reduce the barrier for adoption in existing production lines and may aid scale-up.

In parallel with these manufacturing considerations, building upon the filled voxel concept, there is significant potential to extend to more complex designs, such as lenses with graded refractive index in two or three dimensions, classically exemplified by the Eaton [38] and Luneburg lens [39]. These lenses require precise radial and spherical gradations in refractive index, with a relatively high index ($n \geq 2$) at the center, or in other volumes, for optimal functionality [40]. Compared with conventional porosity-based [18, 19] or standalone ink-extrusion AM approaches [33, 35] that typically yield a limited refractive index range or suffer from composition-lag during continuous ink mixing, the filled voxel technique can enable much higher refractive indices and rapid gradations in high-index regions, minimizing overall system dimensions. Such capabilities could

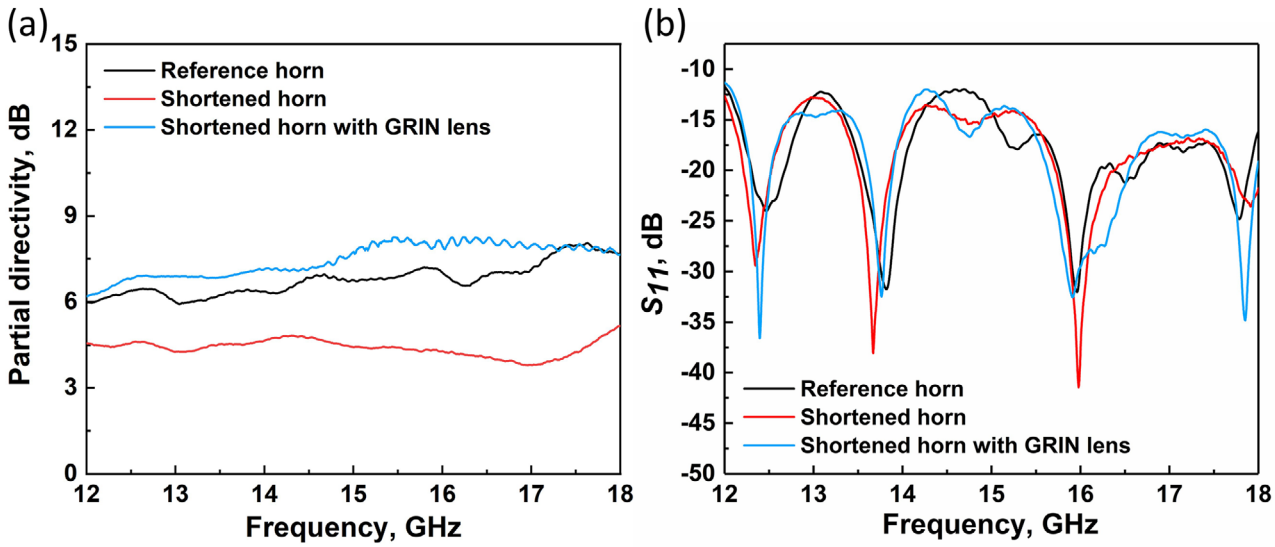

FIGURE 8 | The measured (a) partial directivity and (b) return loss of the reference horn, shortened horn and shortened horn coupled with the GRIN lens.

find application in the design and manufacturing of devices across telecommunications and aerospace sectors.

The filled voxel concept also readily allows for more diverse material types - such as magnetic, conductive, and different phases of materials such as liquids and gases - to be integrated in a single component. This adaptability would allow for more advanced tailoring of electromagnetic, acoustic, or even thermal properties to suit specific applications. For instance, microchannels have been designed that form an internal, interconnected lattice, or repeating 3D pattern of voxels, that were then filled with low melting point Field's metal [41] to create internal circuits or resonating metamaterial structures. Extending this functionality further, the filled voxel concept could be combined with metallic-AM-fabricated lattices, enabling metamaterials with mechanical reinforcement or integrated thermal management [42–44]. Alternatively, filled voxels could be combined with flexible or mechanically deformable lattice frameworks to realize reconfigurable devices whose properties can be tuned dynamically via structural actuation. Such combinations could enable the development of shape-morphing electromagnetic components, wearable systems, or robotic elements with adaptable functionalities.

5 | Conclusions

A hybrid filled voxel AM approach developed for microwave devices that combines additive manufacturing with a palette of standard dielectric sub-voxel composite elements has been successfully demonstrated. The approach has been exemplified for a discretized GRIN lens for a microwave horn. Modeling was used to optimize the discretization of the radial permittivity distribution of the GRIN lens, and then similarly for the sub-voxel arrangement of standardized dielectric materials. The lens was successfully fabricated and experimental performance was in good agreement with simulations. After coupling with the GRIN lens, the overall size of the horn plus lens antenna system was reduced by 50%, while directivity increased from 6.75 dB to 7.74 dB at 15 GHz. The filled voxel concept offers a method to incorporate higher dielectric constant materials into AM than is so far possible from directly printable materials. The concept can also be extended to high permeability, conductive or other functional voxels, and offers a high degree of design freedom in the design, simulation and fabrication of new microwave devices.

6 | Experimental Section

The dielectric composite sub-voxel elements were fabricated using high permittivity $BaTiO_3$ particulate (Sigma–Aldrich, Dorset, UK) and commodity polymer ABS (MFI-22, Styrolution, Germany). Initially, ABS was dissolved in acetone, followed by the addition of 30 vol.% $BaTiO_3$ into the solution, which was then stirred for 12 h to ensure uniform dispersion. After stirring, the solution was dried in a tray, and the resultant solid composite residue was then mechanically milled into smaller pieces using a blade mixer. These fragments were subsequently consolidated into dense 80 mm diameter and 3 mm thick discs in a field-assisted sintering technology (FAST) machine (Dr. Fritsch, DSP 507), operating at 120 °C and 4 MPa for 10 min. The consolidated disc was subsequently mechanically ground to 2 mm uniform thickness before being sectioned into cuboid sub-voxels using a computer numeric control waterjet cutter, as illustrated in Figure 9a. The same process was applied to create the other six types of sub-voxels, with $BaTiO_3$ fractions of 1.5, 5.4, 9.1, 12.9, 16.6, and 20.2 vol%. The internal structure of the sub-voxel composite elements was investigated using X-ray computed tomography (XCT, North Star Imaging Inc.) and scanning electron microscopy (SEM, Zeiss Merlin). The permittivity of the sub-voxels with different $BaTiO_3$ fractions was measured using the split post dielectric resonator (SPDR) method and a Rohde & Schwarz ZNB20 vector network analyzer (VNA) operating at 15 GHz.

The GRIN lattice comprising radial voxels to be filled with stacked sub-voxel composite elements was additively manufactured from polylactic acid (PLA) using a ToolChanger 3D printer (E3D Inc.)

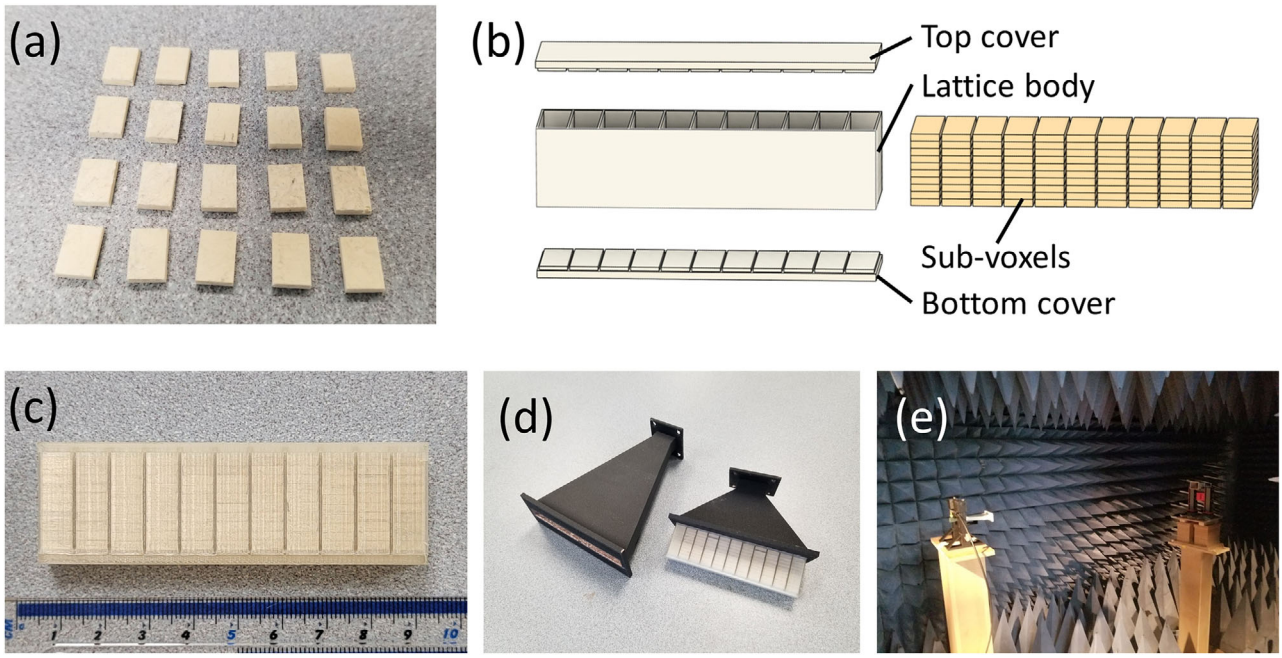

FIGURE 9 | Fabrication and measurement of the filled voxel GRIN lens: a) ABS/$BaTiO_3$ sub-voxel elements prepared by FAST; b) schematic illustration of the assembly showing the lattice body, top and bottom covers, and stacked sub-voxels; c) the assembled filled voxel GRIN lens; d) an AM H-plane horn antenna alongside the shortened horn coupled with the filled voxel GRIN lens; e) the arrangement for the experimental far-field measurement conducted within an anechoic chamber.

via the fused filament fabrication (FFF) method. As shown in Figure 9b, the printed structure consists of three detachable parts: a lattice body, a top cover, and a bottom cover. During assembly, the bottom cover was first attached to the lattice body, after which the sub-voxel elements were manually inserted into each cell with a close sliding fit, leaving an estimated clearance of approximately 0.1 mm between the sub-voxel edges and the lattice walls to ensure repeatable positioning without excessive compression. After all cells were filled, the top cover was aligned and fixed to complete the assembly, forming the finished filled voxel GRIN lens shown in Figure 9c. The stacking configurations used to achieve the desired permittivity profile in each voxel are detailed in Figure S4 (Supporting Information).

The experimental evaluation of the various horn configurations involved measuring angle-dependent far-field transverse electric (TE) polarization radiation patterns within the x-y horizontal plane. Measurements were conducted in an anechoic chamber over a microwave frequency range of 12–18 GHz, utilizing a Rohde & Schwarz ZNB20 VNA in conjunction with transmission and receiving horns. All the horns were printed in carbon fiber filled nylon (Onyx, Markforged) on Markforged Mark Two 3D printer, using standard temperature and layer resolution settings and 0.4 mm diameter nozzles. The inner surfaces of the horns were coated with copper conductive ink by hand (Caswell, USA, 79 $\mu\Omega \cdot$ cm volume resistivity). Figure 9d shows a photograph of the 3D-printed, optimally designed H-plane horn antenna and the shortened horn attached to the filled voxel GRIN lens. The horns were positioned on a synchronized turntable in the anechoic chamber, and the azimuth-plane (horizontal) scanning system is illustrated in Figure 9e, and the distance between the transmitting and receiving horns was maintained at 1.5 m.

Acknowledgements

The authors would like to thank Mr. Robin Vincent and Mr. Gideon Ring for supporting the fabrication of composite voxels.

Conflicts of Interest

The authors declare no conflict of interest.

Data Availability Statement

The data that support the findings of this study are available from the corresponding author upon reasonable request.

References

1. K. Aljaloud, Y. T. Aladadi, M. A. Alkanhal, W. M. Abdulkawi, and R. Hussain, "A wideband GRIN dielectric lens antenna for 5G applications," *Micromachines* 14, no. 5 (2023): 997.

2. S. Zhang, R. K. Arya, S. Pandey, Y. Vardaxoglou, W. Whittow, and R. Mittra, "3D-printed planar graded index lenses," *IET Microwaves, Antennas & Propagation* 10, no. 13 (2016): 1411–1419.

3. X. Xiao, Y. Zhao, X. Ye, et al., "Large-scale achromatic flat lens by light frequency-domain coherence optimization," *Light: Science & Applications* 11, no. 1 (2022): 323.

4. Y. Su and Z. N. Chen, "A radial transformation-optics mapping for flat ultra-wide-angle dual-polarized stacked GRIN MTM Luneburg lens antenna," *IEEE Transactions on Antennas and Propagation* 67, no. 5 (2019): 2961–2970.

5. R. Xu and Z. N. Chen, "A transformation-optics-based flat metamaterial Luneburg lens antenna with zero focal length," *IEEE Transactions on Antennas and Propagation* 70, no. 5 (2022): 3287–3296.

6. W. Hu, C. M. C. Martin, and D. Cavallo, "Design formulas for flat gradient index lenses with planar or spherical output wavefront," *IEEE Transactions on Antennas and Propagation* (2024).

7. S. Zhang, R. K. Arya, W. G. Whittow, D. Cadman, R. Mittra, and J. Vardaxoglou, "Ultra-wideband flat metamaterial GRIN lenses assisted with additive manufacturing technique," *IEEE Transactions on Antennas and Propagation* 69, no. 7 (2020): 3788–3799.

8. J.-M. Poyanco, F. Pizarro, and E. Rajo-Iglesias, "3D-printed dielectric GRIN planar wideband lens antenna for 5G applications," in *2021 15th European Conference on Antennas and Propagation (EuCAP)* (IEEE, 2021), pp. 1–4.

9. J.-M. Poyanco, F. Pizarro, and E. Rajo-Iglesias, "Cost-effective wideband dielectric planar lens antenna for millimeter wave applications," *Scientific Reports* 12, no. 1 (2022): 4204.

10. E. B. Whiting, S. D. Campbell, J. Xu, P. L. Werner, D. H. Werner, J. A. Bossard, J. P. Barrett, J. W. Withrow, and L. Martin, "Topology optimization of RF GRIN lenses," in *2020 IEEE International Symposium on Antennas and Propagation and North American Radio Science Meeting* (IEEE, 2020), pp. 101–102.

11. Z. L. Mei and T. J. Cui, "Experimental realization of a broadband bend structure using gradient index metamaterials," *Optics Express* 17, no. 20 (2009): 18354–18363.

12. H. F. Ma, X. Chen, H. S. Xu, X. M. Yang, W. X. Jiang, and T. J. Cui, "Experiments on high-performance beam-scanning antennas made of gradient-index metamaterials," *Applied Physics Letters* 95, no. 9 (2009).

13. X. Chen, H. Feng Ma, X. Ying Zou, W. Xiang Jiang, and T. Jun Cui, "Three-dimensional broadband and high-directivity lens antenna made of metamaterials," *Journal of Applied Physics* 110, no. 4 (2011).

14. F. Ahmed, K. Singh, and K. P. Esselle, "State-of-the-art passive beam-steering antenna technologies: Challenges and capabilities," *IEEE Access* 11 (2023): 69101–69116.

15. R. Dylla-Spears, T. D. Yee, K. Sasan, et al., "3D printed gradient index glass optics," *Science advances* 6, no. 47 (2020): eabc7429.

16. J. Tu, J. D. Engelhardt, M. H. Barkow, et al., "Additive manufacturing of polymeric gradient index optics via grayscale digital light processing vat photopolymerization technology," *ACS Applied Optical Materials* 3, no. 6 (2025): 1197–1207.

17. A. Žukauskas, I. Matulaitienė, D. Paipulas, G. Niaura, M. Malinauskas, and R. Gadonas, "Tuning the refractive index in 3D direct laser writing lithography: towards GRIN microoptics," *Laser & Photonics Reviews* 9, no. 6 (2015): 706–712.

18. Y. Guo, Y. Li, J. Wang, et al., "A 3D printed nearly isotropic Luneburg lens antenna for millimeter-wave vehicular networks," *IEEE Transactions on Vehicular Technology* 71, no. 2 (2021): 1145–1155.

19. J. Budhu, Y. Rahmat-Samii, R. E. Hodges, D. C. Hofmann, D. F. Ruffatto, and K. C. Carpenter, "Three-dimensionally printed, shaped, engineered material inhomogeneous lens antennas for next-generation spaceborne weather radar systems," *IEEE Antennas and Wireless Propagation Letters* 17, no. 11 (2018): 2080–2084.

20. O. Bjorkqvist, O. Zetterstrom, and O. Quevedo-Teruel, "Additive manufactured dielectric Gutman lens," *Electronics Letters* 55, no. 25 (2019): 1318–1320.

21. D. Isakov, C. J. Stevens, F. Castles, and P. S. Grant, "3D-printed high dielectric contrast gradient index flat lens for a directive antenna with reduced dimensions," *Advanced Materials Technologies* 1, no. 6 (2016): 1600072.

22. L. Wu, X. Tian, M. Yin, D. Li, and Y. Tang, "Three-dimensional liquid flattened Luneburg lens with ultra-wide viewing angle and frequency band," *Applied Physics Letters* 103, no. 8 (2013).

23. H. Han, L. Wu, X. Tian, D. Li, M. Yin, and Y. Wang, "Broadband gradient refractive index planar lens based on a compound liquid medium," *Journal of Applied Physics* 112, no. 11 (2012).

24. M. Feng, X. Tian, J. Wang, M. Yin, S. Qu, and D. Li, "Broadband abnormal reflection based on a metal-backed gradient index liquid slab: an alternative to metasurfaces," *Journal of Physics D: Applied Physics* 48, no. 24 (2015): 245501.

25. M. Yin, X. Yong Tian, L. Ling Wu, and C. Di Li, "All-dielectric three-dimensional broadband Eaton lens with large refractive index range," *Applied Physics Letters* 104, no. 9 (2014).

26. J. Barthel, M. Kleebauer, and R. Buchner, "Dielectric relaxation of electrolyte solutions in acetonitrile," *Journal of Solution Chemistry* 24 (1995): 1–17.

27. B. Allen, T. Pelham, Y. Wu, et al., "Experimental evaluation of 3D printed spiral phase plates for enabling an orbital angular momentum multiplexed radio system," *Royal Society Open Science* 6, no. 12 (2019): 191419.

28. Y. Wu, D. Isakov, and P. S. Grant, "Fabrication of composite filaments with high dielectric permittivity for fused deposition 3D printing," *Materials* 10, no. 10 (2017): 1218.

29. Y. Wu, P. S. Grant, and D. Isakov, "3D-printed $\lambda/4$ phase plate for broadband microwave applications," *Optics Express* 26, no. 22 (2018): 29068–29073.

30. D. Isakov, Y. Wu, B. Allen, P. S. Grant, C. Stevens, and G. Gibbons, "Evaluation of the Laguerre–Gaussian mode purity produced by three-dimensional-printed microwave spiral phase plates," *Royal Society Open Science* 7, no. 7 (2020): 200493.

31. B. W. Lamm, C. L. Cramer, A. Rogers, C. Kumara, and B. L. Armstrong, "Development of direct ink write radially graded alumina/zirconia," Ceramics International 51, no. 27, part C (2025): 54549–54555.

32. O. Rios, W. Carter, B. Post, et al., "3D printing via ambient reactive extrusion," *Materials Today Communications* 15 (2018): 333–336.

33. O. Uitz, R. Leng, T. Pan, et al., "Reactive extrusion additive manufacturing (REAM) of functionally graded, magneto-active thermoset composites," *Additive Manufacturing* 67 (2023): 103486.

34. X. Li, D. Ma, X. Xu, et al., "Graded dielectric metamaterial with designable permittivity fabricated by 3D printing," *Advanced Functional Materials* (2025): e14533.

35. B. Duncan, R. D. Weeks, B. Barclay, et al., "Low-loss graded dielectrics via active mixing of nanocomposite inks during 3D printing," *Advanced Materials Technologies* 8, no. 3 (2023): 2201496.

36. C. A. Balanis, *Antenna theory: analysis and design* (John Wiley & Sons, 2016).

37. D. Meschede, *Optics, light and lasers: the practical approach to modern aspects of photonics and laser physics* (John Wiley & Sons, 2017).

38. S.-H. Kim, "Analytic solution of the generalized Eaton lens," *Journal of Modern Optics* 68, no. 3 (2021): 143–145.

39. Y. Zhao, Y. Zhang, M. Zheng, X. Dong, X. Duan, and Z. Zhao, "Three-dimensional Luneburg lens at optical frequencies," *Laser & Photonics Reviews* 10, no. 4 (2016): 665–672.

40. X. Li, G. Wei, S. Lei, et al., "Bifunctional Luneburg-Eaton lens fabricated of 3-D-printed anisotropic medium," *IEEE Antennas and Wireless Propagation Letters* 21, no. 7 (2022): 1462–1466.

41. C. J. Stevens, I. Spanos, A. Vallechi, J. McGhee, and W. Whittow, "3D printing of functional metal and dielectric composite meta-atoms," *Small* 18, no. 10 (2022): 2105368.

42. C. Ji, K. Li, R. Liao, et al., "Tensile creep mechanisms of laser powder bed fused WE43 alloy with heterogeneous microstructure: Evolution in dislocations and precipitates," *Journal of Materials Science & Technology* 238 (2025): 209–229.

43. B. Li, K. Li, Z. Li, et al., "CMT wire arc additive manufactured ultra-high strength WE43 alloy via in-situ cooling and precipitation regulating," *Materials Research Letters* 13, no. 6 (2025): 596–604.

44. J. Zhan, K. Li, R. Ma, et al., "Achieving fine tailoring of elastocaloric properties of laser powder bed-fused NiTi alloy via laser beam manipulation," *International Journal of Machine Tools and Manufacture* 202 (2024): 104210.

Supporting Information

Additional supporting information can be found online in the Supporting Information section.

Supporting Information